IEEE Access
Multidisciplinary | Rapid Review | Open Access Journal

SPECIAL SECTION ON EMERGING TRENDS, ISSUES AND CHALLENGES FOR ARRAY SIGNAL PROCESSING AND ITS APPLICATIONS IN SMART CITY

Received May 31, 2019, accepted June 24, 2019, date of publication June 28, 2019, date of current version July 19, 2019.

Digital Object Identifier 10.1109/ACCESS.2019.2925739

Near-Field Monopulse DoA Estimation for Angle-Sensitive Proximity WiFi Readers

JOSE ANTONIO LÓPEZ-PASTOR, ANTONIO GÓMEZ-ALCARAZ, DAVID CAÑETE-REBENAQUE, ALEJANDRO SANTOS MARTINEZ-SALA, AND JOSÉ LUIS GÓMEZ-TORNERO, (Senior Member, IEEE)

Department of Information and Communications Technologies, Technical University of Cartagena, 30202 Cartagena, Spain

Corresponding author: José Luis Gómez-Tornero (josel.gomez@upct.es)

This work was supported in part by the Spanish National projects TEC2016-75934-C4-4-R, TEC2016-76465-C2-1-R, and 2018 UPCT Santander Research Grant.

ABSTRACT We study the effect of close-proximity in the estimation of the Direction-of-Arrival (DoA) using a monopulse antenna array system, with application to angle-sensitive proximity WiFi readers. It is shown that in this scenario, it is necessary to consider near-field radiative effects to make an accurate angular estimation at short distances between the mobile terminal and the DoA proximity sensor. As a result, we define a range-dependent angular monopulse function, which provides a better DoA estimation in a Field of View of 60° and for distances ranging from 3 m to 50 cm.

INDEX TERMS Direction-of-arrival, monopulse system, near-field region, proximity detection, WiFi.

I. INTRODUCTION

Proximity sensing of wireless mobile devices is a chief feature for many proximity-based services in the context of the Internet of Things (IoT) in Smart Cities. Among these applications, we can mention proximity-aware activation in smart buildings (such as interactive spaces) [1], machine-to-machine close-physical interaction without human intervention [2], and microlocation at indoor spaces [3]. Although BLE (Bluetooth Low Energy) has been considered as a promising wireless standard for such proximity-based applications due to its low-power, low-cost, low-connectivity range characteristics [4], [5], more recently the WiFi Alliance has defined a new low-power discovery over WiFi standard for proximity applications: the Neighbor Awareness Network also known as WiFi Aware [6]–[8].

Here proximity refers to the relative distance to an object (the sensor), and this should not be confused with indoor location which stands for the absolute position within a given environment. The sensor may be attached to moving objects, and the proximity information may trigger an event depending on the nearness, allowing seamless interaction between a user and the object. In this context, measuring not only the relative distance (ranging) but also the relative direction (angulation), provides richer information for proximity-based contextual services and machine-to-machine physical interaction.

Low-cost proximity ranging estimation with WiFi signals is typically performed from the RSSI (Received Signal Strength Indicator) which can be acquired from WiFi radios, and using indoor propagation models to relate the received power of RF signals to the relative distance between the transmitter and the receiver [9], [10]. ToF (Time-of-flight) based ranging methods [11] are more accurate but at a higher cost due to the need of synchronization (since the estimated distance results from the product of the packet propagation time and the speed of light)

On the other hand, relative angular estimation (also known as DoA, Direction of Arrival) between WiFi devices can be performed using two main signal-processing techniques: phase-based or power-based. As in ranging techniques, more accurate phase-based DoA techniques rely on more complex hardware and signal processing (involving IQ data and synchronization [12]), than power-based DoA techniques which can be applied directly to RSS data [13]. In any case, DoA estimation requires some type of smart antenna array which is capable to measure the inter-element phase or the relative power at different spatial directions [14], [15].

One type of antenna array especially suited for low-cost RSSI-based DoA estimation is the monopulse array, which

The associate editor coordinating the review of this manuscript and approving it for publication was Liangtian Wan.

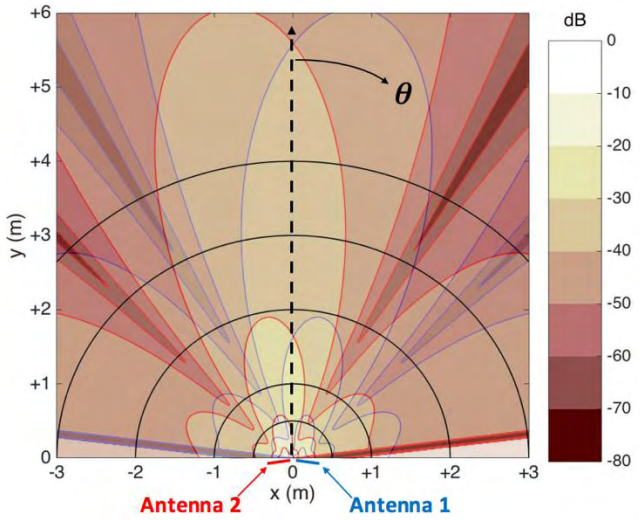

FIGURE 1. Monopulse-array individual radiated field intensity distributions.

was originally applied for long-range RADAR systems [16]. It is basically formed by an array of two antennas producing two directive tilted reference radiation patterns (sketched in Fig.1), which are combined using a monopulse network to derive a sum (Σ) and a difference pattern (Δ). From the relative power levels of these two input channels (Δ / Σ), the DoA can be estimated with high angular resolution in a given Field of View (FoV). Narrower beams provide higher angular resolution but reduced FoV [16].

More recently, the monopulse array concept has been applied for DoA estimation in low-cost Wireless Networks and IoT-related applications, such as 900 MHz band RFID [17]–[20] and 2.45 GHz band WLANs [21]–[24]. In all these cases, the monopulse system provides angular information which cannot be obtained with single-element antennas, and which can be used to add sense of motion and directional information to the conventional proximity reader. Due to its simplicity, the monopulse system is also used in many educational laboratories to teach antenna systems, microwave engineering and signal processing [25]–[29].

In any case, the monopulse-array DoA sensor uses the far-field radiation patterns to characterize the monopulse angular function Δ/Σ , which univocally associates the relative RSS levels to a DoA within the FoV. Still, the far-field assumption might not be accurate for proximity angular sensors, and this could lead to inaccurate DoA estimation. In this work we analyze the near-field effects for a practical monopulse-array sensor designed for WiFi devices in the 2.45 GHz band [24]. Section II describes the theoretical background, showing the near-field effects which appear for distances below 3 meters, and their implications in the monopulse-array technique for DoA estimation. In Section III, a range-dependent near-field monopulse function is defined, which takes into account these effects and provide more accurate DoA predictions at short distances. Finally, Section IV reports experimental validation.

II. THEORETICAL BACKGROUND

A monopulse array synthesizes two partially-overlapped tilted directive radiation patterns, so that any incoming RF signal will create two independent power measurements Δ and Σ, whose relative levels can be univocally related to the angle of DoA. As an example, Fig.1 plots the theoretical radiated-field intensity at 2.45 GHz in the region surrounding the monopulse reader proposed in [24]. It is formed by two commercial WiFi panel antennas (with size 20cm $\times$ 20cm, 14 dBi peak gain and 30° HPBW -Half Power Beam Width- [30]) which are tilted $\pm 7°$ to create the desired partial overlapping.

The fields radiated by antenna 1 (tilt $+7°$) are plotted with blue contours in Fig.1, while the fields of antenna 2 (tilt $-7°$) are plotted with red contours. As it can be seen, the fields radiated by each individual antenna create two well-defined directive beams tilted at $\pm 7°$ to create the desired partial overlapping. It must be remarked that the radiation patterns considered for the design of monopulse systems are usually defined in the far-field regime [16]. It is well-known from antenna theory, that the zone surrounding any antenna can be divided in three distinct regions called the Rayleigh or reactive near-field region (with dominant reactive components of electromagnetic fields), the Fresnel or radiative near-field region (where radiated near fields are dominant but the far-field pattern is not formed yet), and the Fraunhofer or far-field region (where the radiation pattern has a stable angular shape which does not depend on radial distance) [31]. These three zones are delimited by the following expressions:

$$d_{NEARFIELDS} = 0.62 \cdot \sqrt{\frac{S^3}{\lambda}} \tag{1}$$

$$d_{FARFIELDS} = 2 \cdot \frac{S^2}{\lambda} \tag{2}$$

where S stands for the maximum size of the antenna array and λ is the wavelength. In our case with $S = 45$ cm and $\lambda = 12.24$ cm we obtain a far-field limit of 3.3 m and a near-field limit of 53 cm. Therefore, for proximity sensing applications our monopulse array will operate in the Fresnel zone for distances below 3 meters. As it can be seen in the simulated angular patterns plotted in Fig.2, effectively the directive beams of the monopulse array show a stable angular shape for distances above 3 meters. However, as we get in closer proximity to the antenna array, the beams start to distort from their far-field forms. To quantify this effect, the theoretical angle of maximum field intensity is plotted against distance in Fig. 3, showing that only in the Fraunhofer region ($r > 3.3$ m) the beams pointing angle becomes independent on the distance and equal to the designed tilted angle of 7° using far-field theory. In the Fresnel region, the radiated beams direction squints to higher angles, reaching values above 15° in the 50 cm to 1 m range.

Obviously, these near-field beam distortions will impact the monopulse system performance if they are not considered. To evaluate the theoretical effects, the monopulse function

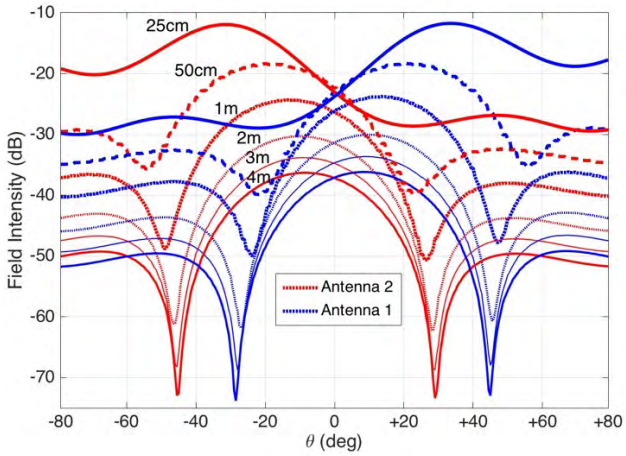

FIGURE 2. Monopulse-array individual field intensity patterns as a function of distance.

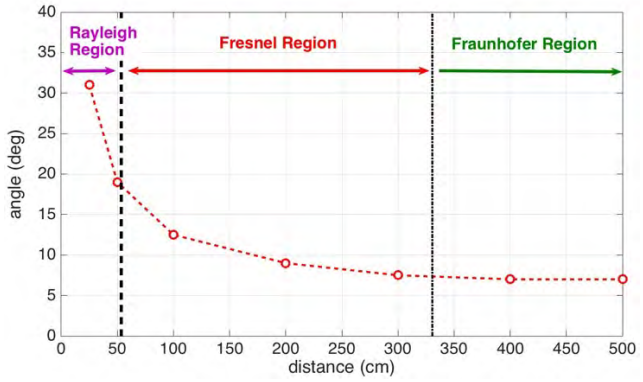

FIGURE 3. Evolution of the peak direction for the monopulse beams in Fig.2 as a function of distance.

(defined as the ratio between the difference Δ and the sum Σ patterns as a function of angle θ), can be analyzed as a function of the radial distance r:

$$\Psi(\theta, r) = \frac{\Delta(\theta, r)}{\Sigma(\theta, r)} \tag{3}$$

Theoretical spatial distributions of the monopulse sum and difference fields in a region close to the monopulse array are plotted in Fig.4. The angular cuts at different radial distances r are shown in Fig.5, where the patterns have been normalized to better compare the relative distortion of their angular shapes as we get in closer proximity to the antenna array.

Effectively, the monopulse patterns become stable only for distances larger than 2 meters. At one-meter distance, the sum pattern Σ starts broadening and the two lobes of the difference pattern Δ start to separate. At 50 cm, the distortion is more pronounced, and the Σ lobe shows a dip at the perpendicular direction ($\theta = 0°$), while the Δ lobes continue splitting away to further directions. At 25 cm, the individual beams totally split away and they do practically not overlap (see Fig.2), and this translates into almost undistinguishable

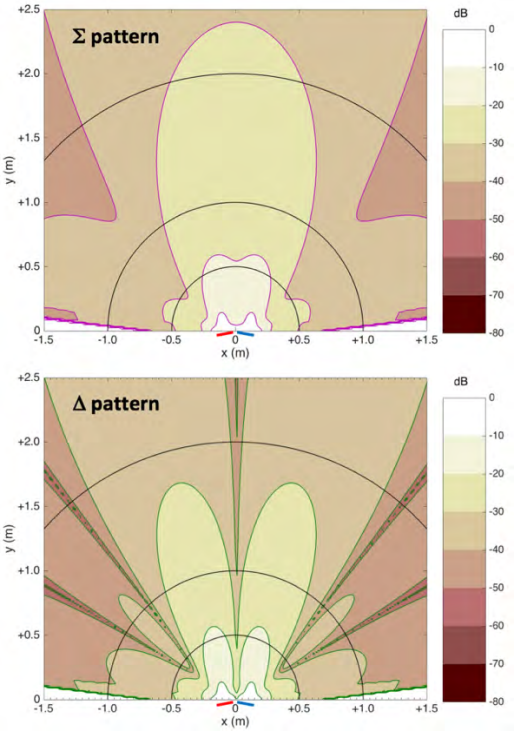

FIGURE 4. Monopulse-array sum (Σ) and difference (Δ) radiated field intensity distributions in the vicinity of the monopulse array.

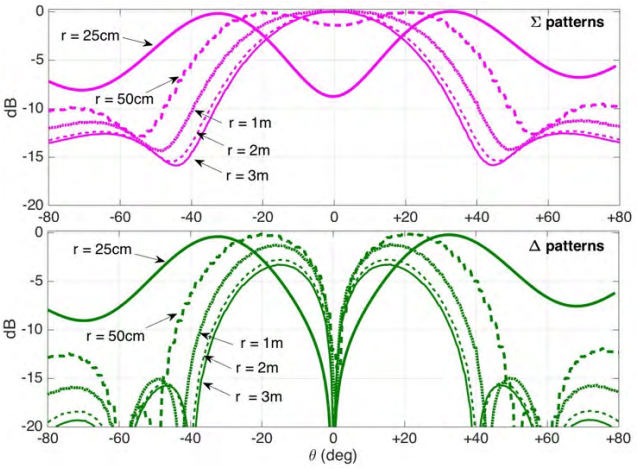

FIGURE 5. Normalized monopulse-array sum (Σ) and difference (Δ) patterns as a function of radial distance.

Σ and Δ patterns but in a narrow angular region around the perpendicular direction.

The resulting angular monopulse function (3) for different radial distances r is plotted in Fig.6. The far-field monopulse function for distances $r > 3$ m shows a Field of View without ambiguity (where there is a unique correspondence between the monopulse function and the DoA) of $\pm 30°$. For $r = 1$ m the near-field monopulse function distorts to a more compressed shape, thus resulting in a lower FoV of $\pm 25°$. This effect becomes more remarkable for $r = 50$ cm showing a FoV below $\pm 20°$. The FoV eventually reduces to very limited angular range of $\pm 10°$ for a close distance $r = 25$ cm, where

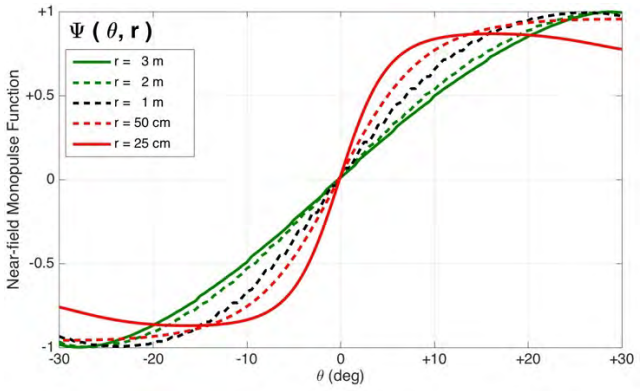

FIGURE 6. Monopulse function (Δ/Σ) at different radial distances.

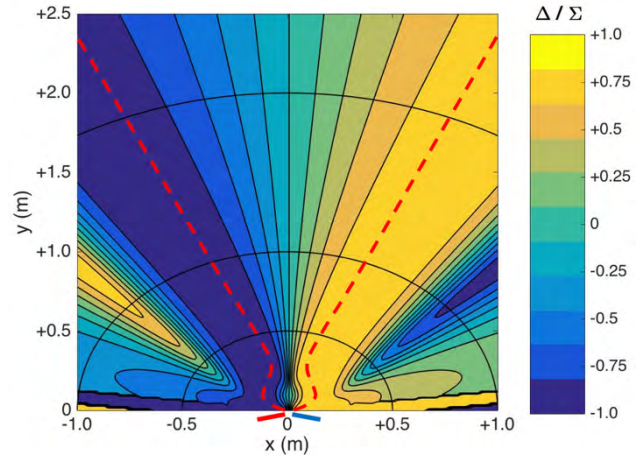

FIGURE 7. Monopulse ratio (Δ/Σ) two-dimensional plot.

the slope of the monopulse function becomes very steep as a consequence of the aforementioned almost total splitting (and no overlapping) of the two individual tilted beams.

The behavior of the monopulse function with the distance is evidenced when the equi-monopulse contour curves are plotted in 2D around the monopulse array, as shown in Fig.7. The FoV zone where the monopulse function presents no ambiguity is enclosed by the red dashed line, showing the aforementioned spatial compression in the close vicinity of the array. Once this near-field electromagnetic behavior has been electromagnetically studied, in the next section we evaluate the practical effects in the estimation of the DoA using the amplitude monopulse technique.

III. DoA ESTIMATION USING DISTANCE-DEPENDENT MONOPULSE FUNCTIONS

Once the RSSI or received power is acquired for both Σ and Δ channels of the monopulse array, the DoA is estimated as:

$$DoA = \theta \xrightarrow{yields} min \left\{ \left| \Psi(\theta, r) - \frac{\Delta_m}{\Sigma_m} \right| \right\} \quad (4)$$

where Σ_m and Δ_m are the power levels measured at the sum and difference channels. As it can be seen, Eq. (4) depends on the distance r selected to estimate the DoA, since the

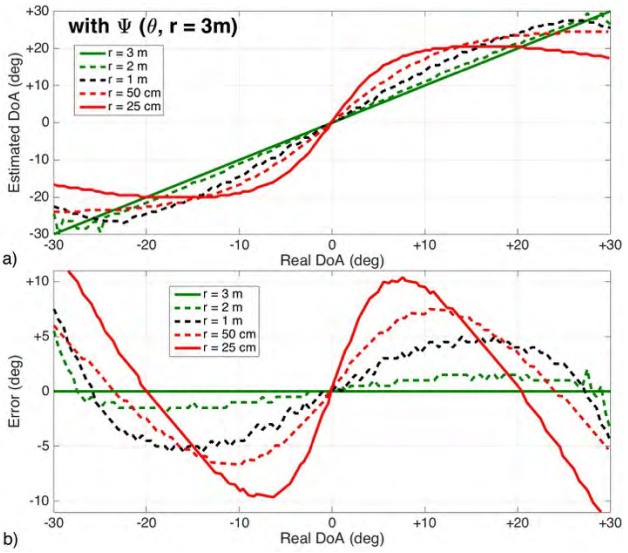

FIGURE 8. Theoretical DoA estimation for different radial distances, using the monopulse function characterized at $r = 3$ m.

monopulse function has proved to be dependent on distance in the near-field range. Typical monopulse systems operate in the far-field region and therefore a unique monopulse function can be used to estimate the DoA, independently on the radial distance.

This is not true for the case of proximity sensors, as it is illustrated in Fig.8a where the DoA is estimated at different distances r and using the monopulse function characterized for a far-field distance of $r = 3$m. The corresponding estimation error is plotted in Fig.8b. As shown in Fig.8, the theoretic DoA estimation is perfect and the error is null when the target is located at $r = 3$m, which coincides with the distance used to characterize the monopulse function. However, as the target gets closer to the monopulse array, the DoA estimated using the far-field monopulse function is less accurate, showing an angular error of $\pm 5°$ for $r = 1$ m, which increases to $\pm 7°$ for $r = 50$ cm, and up to $\pm 10°$ for $r = 25$ cm. Therefore, it is proved that the far-field patterns cannot provide accurate monopulse DoA estimation in the near-field range.

In Fig.9, a similar DoA estimation test is performed but now using the monopulse function characterized at a near-field distance of $r = 50$ cm. Now, the estimation error is zero when the target moves in this calibration near-field distance of 50 cm. The DoA estimation becomes more inaccurate as the target moves to further distances into the far-field zone. A maximum DoA estimation error of $\pm 7°$ is observed at a far distance of $r = 3$ m, when using the near-field monopulse function characterized at the distance of $r = 50$ cm. Besides, it must also be remarked that in the near-field zone, the FoV is compressed to $\pm 15°$ (see Fig.6), so that the DoA estimation error strongly increases out from this limited angular zone, as shown in Fig.9. These results demonstrate that, for accurate DoA estimation using the monopulse technique in the near-field zone, it is needed a range-dependent monopulse function (3) which takes into account the fluctuations observed in the monopulse patterns as a function of distance.

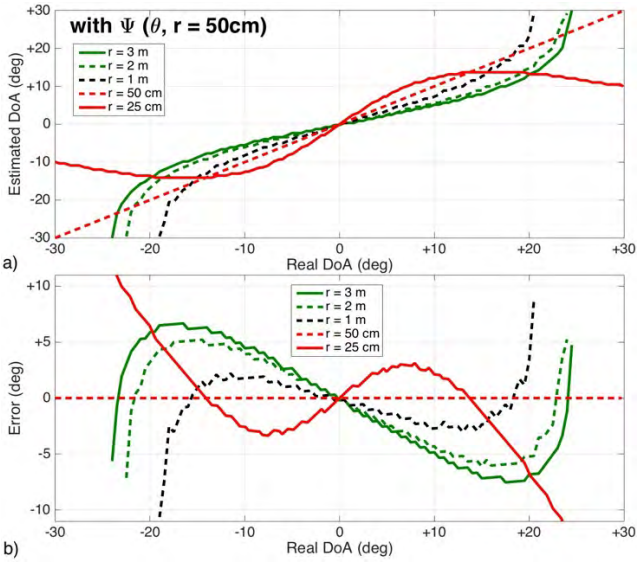

FIGURE 9. Theoretical DoA estimation for different radial distances, using the monopulse function characterized at $r = 50$ cm.

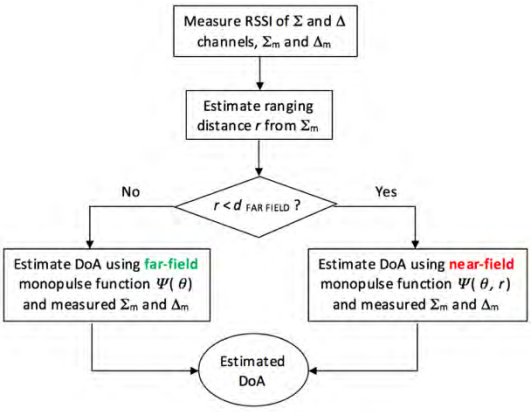

FIGURE 10. Flow chart for range-dependent DoA estimation.

In Fig.10, we propose a distance-dependent monopulse DoA estimation algorithm. First, the distance r between the proximity sensor and the mobile device is estimated from the RSSI acquired at the sum channel Σ_m, and using RSSI-based ranging techniques [9], [10]. If the mobile is located in the far-field zone $r > d_{\text{FARFIELD}}$ given by (2), the conventional far-field monopulse function which is not dependent on distance can be applied to estimate the DoA. However, if the mobile is in the near-field range, the more satisfactory near-field monopulse function $\Psi(\theta, r)$ (3) must be applied to accurately estimate the DoA at the calculated distance r.

Another scenario where the near-field monopulse function must be used is the one in which the perpendicular distance between the proximity sensor and the mobile is fixed and previously known. This happens in corridor-like, conveyor belt and security gates scenarios, when the sensor is ceiling-mounted at a given height, or when the sensor is mounted on a wall at a security distance from the corridor, as shown in Fig.11. In these cases, the distance H is fixed and known

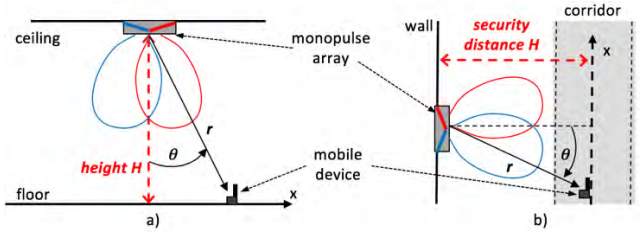

FIGURE 11. Corridor-like scenarios with constant perpendicular distance H a) Lateral view of monopulse mounted on ceiling at height H b) Top view of monopulse mounted on wall with lateral security distance H.

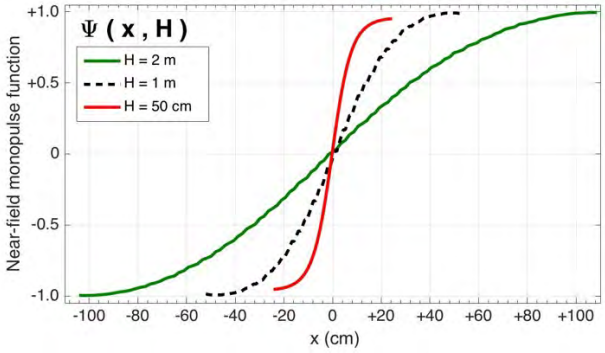

FIGURE 12. Near-field monopulse functions for different perpendicular distances H as a function of longitudinal position x.

a priori, and the mobile moves only in one direction x. As the mobile moves along different positions x, the distance$r$ and the DoA angle θ are geometrically related as:

$$r = \frac{H}{cos\theta}; \quad x = H \cdot tan\theta \tag{5}$$

Therefore, in these cases it is practical to define a near-field monopulse function which depends on x for any value of H, and which allows to estimate the relative Cartesian shift x:

$$\Psi(x, H) = \frac{\Delta(x, H)}{\Sigma(x, H)} \tag{6}$$

This is shown in Fig.12 for different distances H. It must be noticed that these near-field monopulse functions are calculated taking into account that, for each longitudinal position x, not only the subtending angle θ varies, but also the radial distance r changes according to (5). As shown in Fig.12, lower values of H shorten the longitudinal zone which can be sensed, referred to as the longitudinal FoV (LFoV) in cm. The LFoV in the x direction reduces from 2 meters for $H = 2$ m, to LFoV $= 90$ cm for $H = 1$ m, and to LFoV $= 40$ cm for $H = 50$ cm. These results are in accordance with the 2D monopulse FoV plots previously showed in Fig.7.

On the other hand, higher spatial resolution is obtained for lower distances H, as it can be seen from the steep slope of the monopulse function $\Psi(x)$ for $H = 50$ cm in Fig.12. In any case, the near-field monopulse functions take into account the near-field effects for an accurate angular position estimation. In the following Section, we experimentally corroborate these theoretical results using a practical WiFi monopulse sensor operating in the near-field zone.

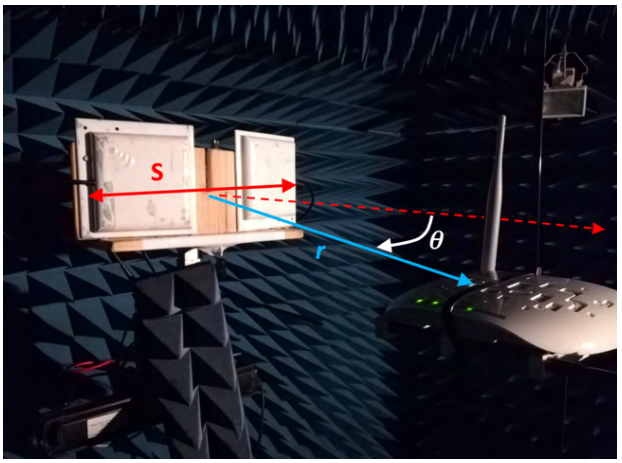

FIGURE 13. Picture of WiFi monopulse sensor [24] tested in chamber.

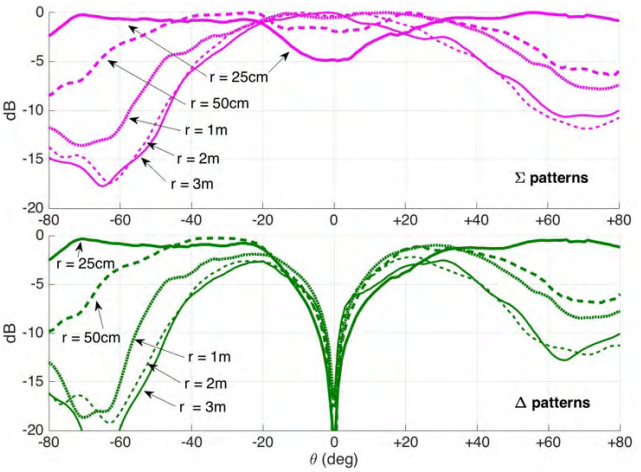

FIGURE 14. Measured RSSI levels at the sum (Σ) and difference (Δ) channels of the WiFi monopulse-array as a function of angle and radial distance.

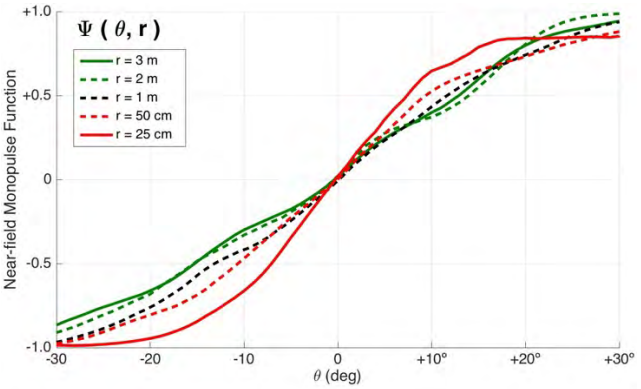

FIGURE 15. Measured near-field digital monopulse functions.

IV. EXPERIMENTAL VALIDATION

A practical monopulse array for WiFi DoA estimation designed in [24], is characterized in the near-field zone. The antenna array has a maximum dimension $S = 45$ cm -depicted in Fig.13- and operates in the WiFi 2.45 GHz band. Therefore, all previous theoretical results apply, and the near-field radiation range is limited between 50 cm and 3.3 m.

The monopulse system is tested in an anechoic chamber. A WiFi Access Point (AP) is configured to continuously send WiFi beacon frames, every 100 msec. and with 0 dBm power using channel 6 (2.437 GHz). In this way, we ensure a reference transmitter with constant emitted power and permanent traffic. The monopulse antenna is connected to a WiFi MiMo card which sniffs WiFi frames as explained in [24]. The RSSI levels of WiFi frames received at the sum Σ and difference Δ monopulse channels, are measured as a function of angle for different radial distances ($r = 3$ m, 2 m, 1 m, 50 cm and 25 cm). As shown in Fig.14, the measured RSSI angular patterns are in good agreement with the theoretical radiation patterns (Fig.5), demonstrating the expected near field distortion. As we get in close proximity to the array, the Σ and Δ patterns broaden, and eventually a dip is created in the perpendicular direction ($\theta = 0°$) of the sum pattern Σ.

The corresponding digital (WiFi RSSI-based) monopulse functions as a function of radial distance r, are plotted in Fig.15. Again, good agreement is found between experiments and theory. As expected, the monopulse function is not stable with distance due to the near-field effects, showing a steeper angular slope and a narrower FoV as we approximate to the antenna array, in accordance with the theoretical plots in Fig.6.

Using these near-field monopulse functions $\Psi(\theta, r)$, the DoA can be estimated for different distances. To avoid multipath effects, the first DoA estimation experiments are performed inside the anechoic chamber. Fig.16 shows the measured DoA estimation error using the far-field monopulse function (the one in Fig.15 for $r = 3$ m), while approaching the antenna array. The dots in Fig.16 represents different error measurements at distinct angular positions inside the anechoic chamber, while the average error is plotted with a solid line. The RMSE (root mean square error) of the DoA estimation for each distance in Fig.16 is summarized in the first row of Table 1. It must be noticed that the WiFi monopulse reader reports an angular uncertainty of $\pm 2.5°$ due to digital quantization of RSSI digital levels [24]. This creates a systematic error which limits the resolution to this $\pm 2.5°$ value as shown in Fig.16 for a measuring distance $r = 3$ m, and corresponding to a RMSE of only 0.7°. Then, the estimation error increases as we get in closer proximity to the array due to the near-field effects. Experiments are in good concordance with theoretical results shown in Fig.8. For $r = 1$ m, the angular peak error augments in a extent of 3° thus creating an accumulated peak error of $\pm 5°$ (RMSE 2°), which increases to $\pm 7°$ for $r = 50$ cm, and up to $\pm 11°$ for $r = 25$ cm (RMSE 6°).

If we use the near-field monopulse function for $r = 50$ cm, the DoA estimation errors are plotted in Fig.17 at different distances. The RMSE for these experiments are summarized in the fourth row of Table 1. As expected, the minimum error (RMSE 1.4°) is obtained when the mobile device is located at this nearby distance of 50 cm. In accordance with the

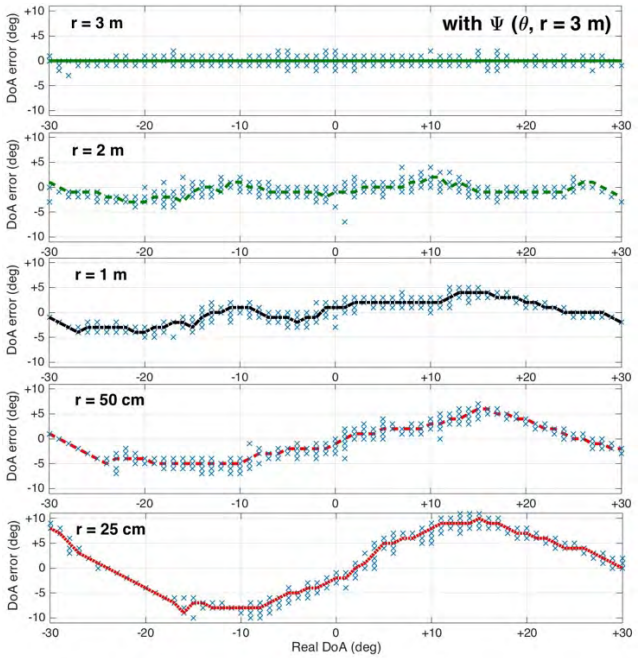

FIGURE 16. Measured DoA estimation error for different radial distances, using the monopulse function characterized at $r = 3$ m.

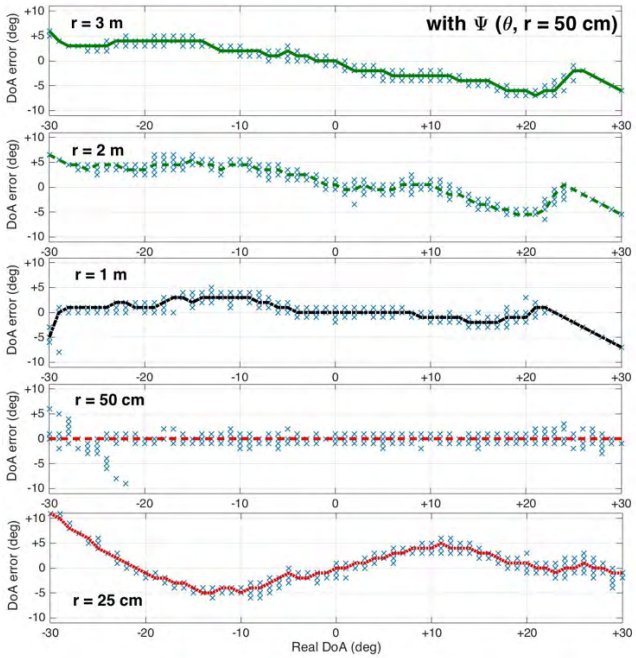

FIGURE 17. Measured DoA estimation error for different radial distances, using the monopulse function characterized at $r = 50$ cm.

TABLE 1. RMSE of DoA estimation (deg) as a function of radial distance r.

Monopulse function	measuring distance r, FoV = 60º				
	3 m	2 m	1 m	50 cm	25 cm
$\Psi(\theta, r{=}3m)$	0.7 º	1.7 º	2.0 º	3.6 º	6.0 º
$\Psi(\theta, r{=}2m)$	1.7 º	1.0 º	2.1 º	3.5 º	6.2 º
$\Psi(\theta, r{=}1m)$	1.9 º	2.1 º	0.9 º	2.0 º	4.5 º
$\Psi(\theta, r{=}50cm)$	3.6 º	3.5 º	2.2 º	1.3 º	3.4 º
$\Psi(\theta, r{=}25cm)$	5.9 º	6.1 º	4.4 º	3.7 º	1.4 º

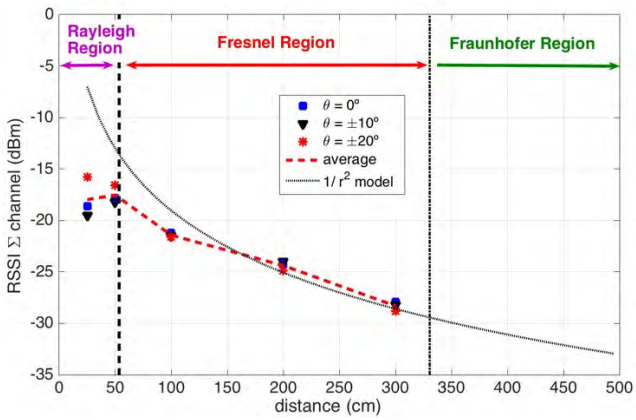

FIGURE 18. Measured RSSI level at Σ channel as a function of distance.

theoretical plots in Fig.9, this error increases as we move away from the array. A maximum RMSE of 3.6° is now observed for the further distance of $r = 3$ m due to the near-to-far field aberration effects. In the closest distance of $r = 25$ cm, the estimated DoA presents a RMSE of 3.4°. It must be noticed that this error at 25 cm using the near-field monopulse function for $r = 50$ cm, is lower than the one of 6.0° reported when using the far-field monopulse function with $r = 3$ m.

Also, it must be noticed that the mean error curves plotted with lines in Fig.16 and 17, follow the predicted dependence with the angle of observation for all the performed tests (see theoretical plots in Fig.8b and Fig.9b, respectively). Basically, the mean error is null at boresight direction (DoA 0°), and increases for higher angular directions. In any case, the best DoA estimation performance for any distance r in the entire FoV, is obtained when the adequate monopulse function is used, as highlighted in green color in Table 1.

To mitigate the DoA estimation inaccuracies due to near-field effects, we implement the range-dependent monopulse estimation algorithm sketched in Fig.10. The acquired RSSI level at the sum pattern Σ, for different measuring distances and angles is shown in Fig.18. Also, the curve obtained from a simple spherical-wave propagation model is plotted for reference. From the measured RSSI level and using the average curve plotted in red, the radial distance r can be anticipated to use the appropriate monopulse function $\Psi(\theta, r)$.

The result of this range-dependent DoA estimation is plotted in Fig.19. The obtained RMSE values correspond to the data highlighted in green in the diagonal of Table 1. Now, for any distance ranging from 3 m to 25 cm, all the individual experiments show an RMSE below 1.5° at any direction within the FoV. The averaged DoA estimation error plotted in Fig.19 is null at any distance when using the appropriate monopulse function. As explained in [24], the RSSI levels

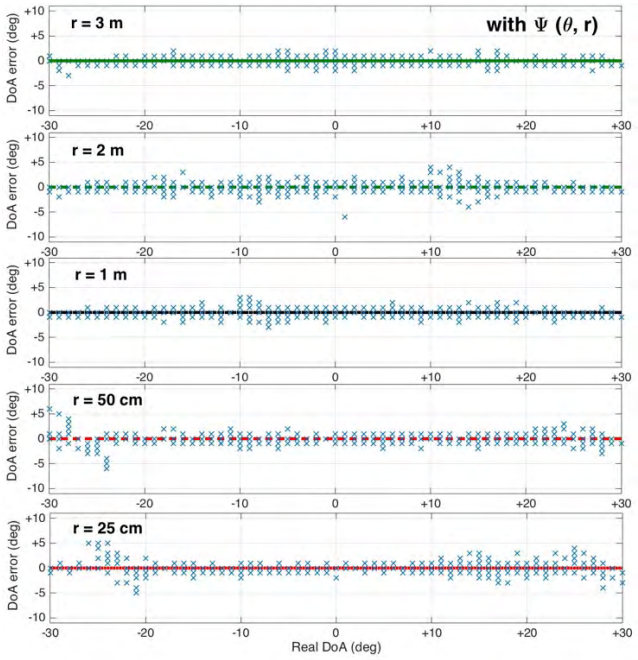

FIGURE 19. Measured DoA estimation error for different radial distances, using the corresponding range-dependent monopulse functions.

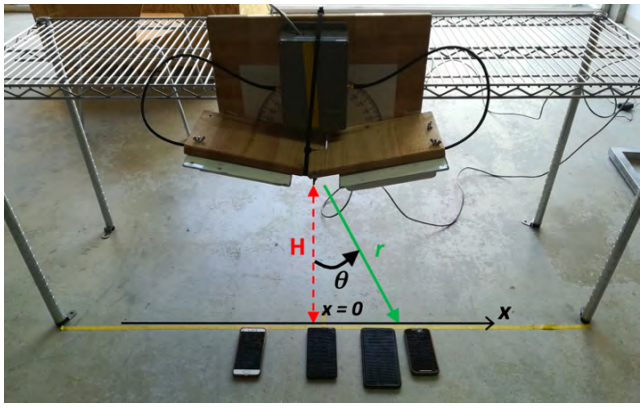

FIGURE 20. Picture of WiFi angle-sensitive proximity sensor mounted in a security shelf.

are discretized in 1-dBm steps, and this creates oscillations of ±2.5° in the DoA estimation around this null average error.

If the near-field effects are not considered and it is used the conventional monopulse function for far-field angular estimation (as done in long-range RADARs [16]), the average angular error plotted in Fig.16 can increase up to 11° at short distances, with corresponding RMSE growing up to 6° as summarized in Table 1.

Once it has been demonstrated in an anechoic chamber the necessity to consider the near-field effects to estimate the DoA for short distances, a practical outdoor scenario as the one shown in Fig.20 is tested. As it was sketched in Fig.11a, security-gate proximity sensors can be ceiling-mounted at a given height H. In our case we have located the proximity angular sensor on a security shelf, at a short height H from the mobile WiFi devices to be sensed.

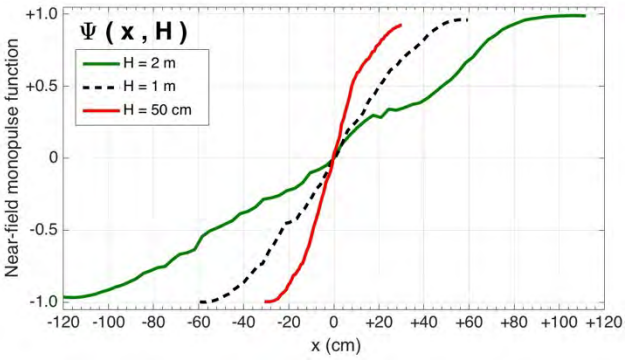

FIGURE 21. Measured near-field monopulse functions as a function of longitudinal position x, for different perpendicular distances H.

The near-field longitudinal monopulse function $\Psi(x,H)$ (6) characterized in the anechoic chamber at three different distances $H = 2$ m, 1 m and 50 cm are plotted in Fig.21. As expected from theory (see Fig.12,), the longitudinal FoV (LFoV) narrows and the spatial resolution (slope) increases as the height H is shortened. These functions are used to estimate the position of three different WiFi devices: the same AP used in the anechoic chamber (see Fig.13), and two smartphones as illustrated in Fig.20.

The WiFi packets transmitted by the mobile devices are collected by the WiFi monopulse reader, which compares the measured sum and difference RSSI values (Σ_m and Δ_m), with the near-field monopulse function $\Psi(x,H)$ to estimate the x position:

$$Position = x \overset{yields}{\longrightarrow} min\left\{\left|\Psi\left(x,H\right) - \frac{\Delta_m}{\Sigma_m}\right|\right\} \qquad (7)$$

In a first experiment, the WiFi monopulse reader is mounted at a height $H = 50$ cm above the floor, so that a LFoV of ±25 cm can be sensed. The three mobile devices (access point, smartphone 1 and smartphone 2) are located at different x positions within this LFoV. Fig. 22 shows the estimation error in cm for the three WiFi mobile devices under test, and using monopulse functions characterized at different heights. Table 2 summarizes the RMSE in the location estimation. Accurate proximity location with peak errors below ±6 cm in the entire 50 cm LFoV and a with a RMSE value below 4 cm, is obtained for the three devices when the appropriate near-field monopulse function $\Psi(x, H = 50$ cm) is used. However, if we use the monopulse function characterized for $H = 1$ m the peak errors increase up to ±25 cm (RMSE 18.5 cm), and up to ±70 cm (RMSE 57 cm) when using the monopulse for $H = 2$ m.

The experiment is repeated for a higher distance $H = 1$m, reporting the results in Fig.23 in an extended LFoV of ±55 cm in the x direction. Now, the most accurate position estimations are obtained when the correct near-field monopulse function $\Psi(x, H = 1$ m) is chosen, showing a maximum peak error of ±15 cm (RMSE below 6.8 cm) for any of the three studied WiFi devices. As expected, the minimum error has increased for this higher H when compared

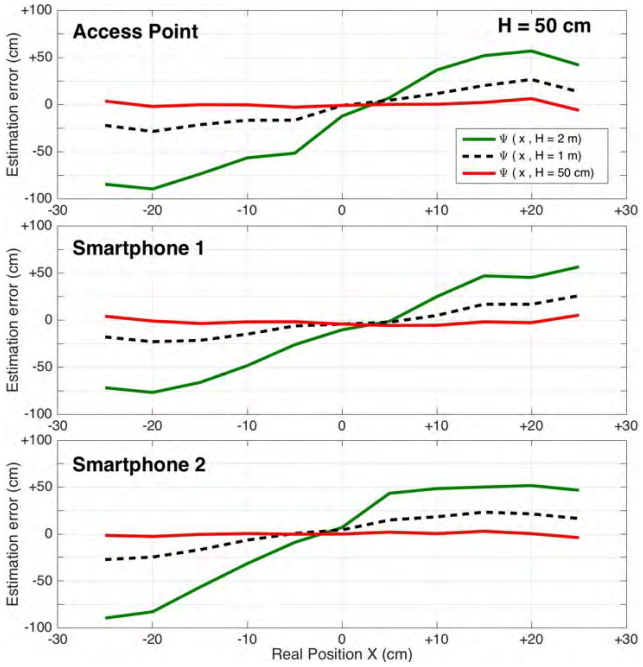

FIGURE 22. Position estimation error for the set-up in Fig.20 with $H = 50$cm.

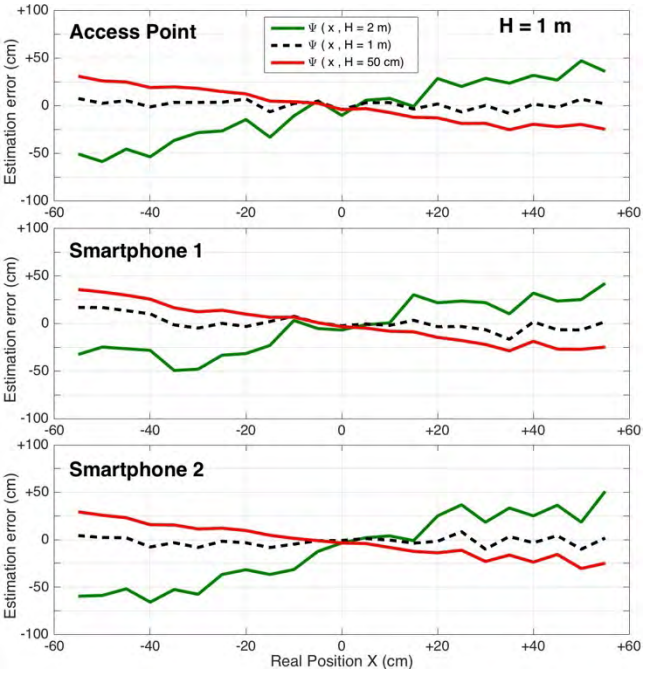

FIGURE 23. Position estimation error for the set-up in Fig.20 with $H = 1$m.

TABLE 2. RMSE of position estimation (cm) as a function of height H and for three different WiFi devices.

Monopulse function	measuring height H = 50 cm, LFoV = 50 cm		
	Access Point	Smartphone1	Smartphone2
$\Psi(x, H{=}2m)$	57.0 cm	52.9 cm	49.2 cm
$\Psi(x, H{=}1m)$	18.5 cm	17.9 cm	16.1 cm
$\Psi(x, H{=}50cm)$	3.1 cm	1.8 cm	3.8 cm
Monopulse function	measuring height H = 1 m, LFoV = 110 cm		
	Access Point	Smartphone1	Smartphone2
$\Psi(x, H{=}2m)$	31.9 cm	38.1 cm	27.3 cm
$\Psi(x, H{=}1m)$	4.4 cm	5.1 cm	6.7 cm
$\Psi(x, H{=}50cm)$	17.9 cm	17.0 cm	19.9 cm

TABLE 3. Near-field ranges of reported monopulse systems used for IoT applications.

Ref.	frequency	Monopulse array size S	$d_{\text{NEARFIELD}}$ (1)	d_{FARFIED} (2)	FoV
[17]	867 MHz	54 cm	42 cm	1.7 m	±40º
[18]	915 MHz	37 cm	24 cm	83 cm	±30º
[19]	920 MHz	18 cm	8 cm	20 cm	±20º
[20]	868 MHz	60 cm	49 cm	2 m	±40º
[21]	2.3 GHz	30 cm	28 cm	1.3 m	±45º
[22]	2.45 GHz	9 cm	5 cm	14 cm	±45º
[23]	2.45 GHz	30 cm	30 cm	1.5 m	±40º
[24]	2.45 GHz	45 cm	50 cm	3.3 m	±30º

to the case $H = 50$ cm, due to the lower resolution of $\Psi(x, H)$ -lower slopes in Fig.21- as H rises. This error growths if the correct monopulse function is not selected, as it can be seen in Fig.23 for the cases $\Psi(x, H = 2$ m) and $\Psi(x, H = 50$ cm), which report higher location errors of ±65 cm (RMSE 38.1 cm) and ±35 cm (RMSE 19.9 cm), respectively. In all cases, the estimation errors in Figs. 22 and 23 are higher for locations away from the perpendicular direction of the sensor, following the tendency shown for the DoA estimation error in Figs. 16 and 17.

Therefore, it has been proved that the studied angular-sensitive monopulse sensor can provide accurate directional proximity estimation if the appropriate near-field monopulse functions are considered. The system is able to estimate the actual location within a root mean square error below 4 cm in the entire LFoV of 50 cm for a near-field height of $H = 50$ cm, and with an RMSE below 7 cm for $H = 1$ m, and for any of the three WiFi devices as highlighted in green in Table 2. Far-field assumptions are not valid at these close distances, leading to high DoA estimation errors and thus considerable proximity location inaccuracies.

For the authors' knowledge, it is the first time that the amplitude-monopulse angular estimation technique is applied for near-field angular-sensitive proximity detection. As summarized in Table 3, the near-field region of many of the monopulse systems proposed in recent designs for RFID/ WLANs systems, extends to a remarkable range of distances where these near-field effects cannot be ignored. The extension of the near-field zone is enlarged as the antenna size is greater, as happens for directive-beamed arrays which

provide high DoA resolution as the one studied in this paper. As done in near-field RFID antennas [32], [33], it is important to consider the near-field effects to predict the actual digital reading performance of directive proximity sensors.

V. CONCLUSION

The estimation of the direction of arrival (DoA) using monopulse techniques, has been studied for the case of proximity angular sensors. The amplitude monopulse technique offers simplicity to estimate the DoA with good angular resolution, using RSSI information which is directly available using commodity hardware and a low-cost array of two directive antennas. However, monopulse systems have been typically used in the far-field zone of the antenna array (for instance in long-range monopulse RADAR systems), where the monopulse function is stable with distance. As demonstrated in this paper, this is not the case for monopulse sensors used in proximity-aware applications for Smart Spaces, where the IoT / smartphones mobile devices can be in the near-field zone of the monopulse array.

The near-field effects in the proximity of a practical angle-sensitive proximity WiFi monopulse array operating in the 2.45 GHz band have been evaluated. The experimental results are consistent with electromagnetic theory, showing that far-field sum and difference patterns distort in the proximity of the sensor, making the monopulse functions strongly dependent on the radial distance. It has been shown that high DoA estimation errors of more than 10° appear close to the sensor, if the conventional far-field monopulse function is used when sensing in the near-field radiative zone (which in our case extends from 50 cm to 3 meters from the array). Thus we have proposed the use of a range-dependent near-field monopulse function $\Psi(\theta,r)$ which takes into account the near-field range effects, and estimates the DoA with higher accuracy.

Similarly, the monopulse function can be defined in Cartersian near-field coordinates, i.e. $\Psi(x,H)$, to estimate the proximity position x with good accuracy in the immediacy of the monopulse array. For that, the perpendicular distance H must be fixed and known, as happens in security gates. These concepts have been experimentally demonstrated with a practical angle-sensitive proximity WiFi sensor, proving the mitigation of the near-field aberration effects to estimate with accuracy the direction and contiguity location of mobile devices at close distances from the monopulse array.

The proposed technique has proved a DoA estimation root mean square error below 1.5° in a FoV of 60°, and for a range of distances from 50 cm to 3 meters of the sensor. This translates to a root mean square error below 4 cm over a linear FoV of 50 cm, when locating real WiFi devices from a height of $H = 50$ cm. The location RMSE increases to 7 cm when covering a wider linear FoV of 110 cm from a height of $H = 1$ m. Although the results of this paper have been applied for a particular WiFi monopulse proximity sensor, the reported considerations are valid for any monopulse system operating in the near-field zone, and using any alternative wireless technology such as Bluetooth, Zigbee or RFID.

REFERENCES

[1] M. Hadian, T. Altuwaiyan, X. Liang, B. Sheng, and K. Zhang, "SmartEye: Mobile device proximity monitoring via wireless signal analysis," in *Proc. Int. Conf. Comput., Netw. Commun. (ICNC)*, Honolulu, HI, USA, Feb. 2019, pp. 365–369.

[2] T. J. Pierson, T. Peters, R. Peterson, and D. Kotz, "Proximity detection with single-antenna IoT devices," in *Proc. ACM Int. Conf. Mobile Comput. Netw. (MobiCom)*, Oct. 2018, pp. 663–665.

[3] P. Spachos, I. Papapanagiotou, and K. N. Plataniotis, "Microlocation for smart buildings in the era of the Internet of Things: A survey of technologies, techniques, and approaches," *IEEE Signal Process. Mag.*, vol. 35, no. 5, pp. 140–152, Sep. 2018.

[4] M. S. Gast, *Building Applications With iBeacon: Proximity and Location Services With Bluetooth Low Energy*. Sebastopol, CA, USA: O'Reilly Media, 2014.

[5] K. E. Jeon, J. She, P. Soonsawad, and P. C. Ng, "BLE beacons for Internet of things applications: Survey, challenges, and opportunities," *IEEE Internet Things J.*, vol. 5, no. 2, pp. 811–828, Apr. 2018.

[6] *WiFi Aware Networking Specification From WiFi Alliance—Draft 15*, Wi-Fi Alliance, Austin, TX, USA, 2018.

[7] Craig Mathias. *WiFi and the Internet of Things: Much More Than You Think*. Accessed: Jun. 2019. [Online]. Available: https://www.wi-fi.org/beacon/craig-mathias/wi-fi-and-the-internet-of-things-much-more-than-you-think

[8] S. Saloni and A. Hegde, "WiFi-aware as a connectivity solution for IoT pairing IoT with WiFi aware technology: Enabling new proximity based services," in *Proc. Int. Conf. Internet Things Appl. (IOTA)*, Pune, India, Jan. 2016, pp. 137–142.

[9] Y. Zhao, M. Li, and F. Shi, "Indoor radio propagation model based on dominant path," *Int. J. Commun. Netw. Syst. Sci.*, vol. 3, no. 3, pp. 330–337, 2010.

[10] A. Zanella, "Best practice in RSS measurements and ranging," *IEEE Commun. Surveys Tuts.*, vol. 18, no. 4, pp. 2662–2686, 4th Quart., 2016.

[11] D. Macii, F. Trenti, and P. Pivato, "A robust wireless proximity detection technique based on RSS and ToF measurements," in *Proc. IEEE Int. Workshop Meas. Netw. (M&N)*, Anacapri, Italy, Oct. 2011, pp. 31–36.

[12] J. Gjengset, J. Xiong, G. McPhillips, and K. Jamieson, "Phaser: Enabling phased array signal processing on commodity WiFi access points," in *Proc. 20th Annu. Int. Conf. Mobile Comput. Netw. MobiCom*, 2014, pp. 153–164.

[13] S. Maddio, A. Cidronali, and G. Manes, "RSSI/DoA based positioning systems for wireless sensor network," in *New Approach of Indoor and Outdoor Localization Systems*. Rijeka, Croatia: InTech, 2012, pp. 139–162.

[14] C. L. Godara, "Application of antenna arrays to mobile communications, Part II: Beam-forming and direction-of-arrival considerations," *Proc. IEEE*, vol. 85, no. 8, pp. 1195–1245, Aug. 1997.

[15] L. Brás, N. B. Carvalho, P. Pinho, L. Kulas, and K. Nyka, "A review of antennas for indoor positioning systems," *Int. J. Antennas Propag.*, vol. 2012, Oct. 2012, Art. no. 953269.

[16] S. M. Sherman and D. K. Barton, *Monopulse Principles and Techniques*. Norwood, MA, USA: Artech House, 2011.

[17] R. Parada, A. Carreras, J. Melià-Seguí, and R. Pous, "Study of a monopulse system with RFID antennas for applications oriented to retail industry," in *Proc. ACM Conf. Pervasive Ubiquitous Comput. Adjunct Publication (UbiComp)*, New York, NY, USA, 2013, pp. 279–282.

[18] C. Alcaraz, J. V. Balbastre, and F. Vega, "Monopulse RFID reader for enhanced intelligent transportation systems applications," in *Proc. IEEE Brazil RFID*, Sao Paulo, Brazil, Oct. 2015, pp. 1–4.

[19] T. Sakogawa, K. Aoki, and F. Kuroki, "A technique to narrow down radiation patterns of broad beam antenna operationally and its application to security gate to prevent shoplifting based on monopulse system," in *Proc. 11th Eur. Conf. Antennas Propag. (EUCAP)*, Paris, France, Mar. 2017, pp. 1945–1948.

[20] Y. Á. López, M. E. de Cos Gómez, and F.-H. Andrés, "A received signal strength RFID-based indoor location system," *Sens. Actuators A, Phys.*, vol. 255, pp. 118–133, Mar. 2017.

[21] J.-C. Wu, C.-C. Chang, T.-Y. Chin, S.-H. Chang, M.-C. Chiu, C.-Y. Hsu, and R.-H. Lee, "Wireless indoor localization using dynamic monopulse receiver," in *Proc. EURAD*, Sep./Oct. 2010, pp. 69–72.

[22] M. D. Prete, D. Masotti, N. Arbizzani, and A. Costanzo, "Remotely identify and detect by a compact reader with mono-pulse scanning capabilities," *IEEE Trans. Microw. Theory Techn.*, vol. 61, no. 1, pp. 641–650, Jan. 2013.

[23] N. Honma, K. Ishii, Y. Tsunekawa, H. Minamizawa, and A. Miura, "DOD-based localization technique using RSSI of indoor beacons," in *Proc. Int. Symp. Antennas Propaga. (ISAP)*, Nov. 2015, pp. 923–924.
[24] J. L. Gómez-Tornero, D. Cañete-Rebenaque, J. A. López-Pastor, and A. S. Martínez-Sala, "Hybrid analog-digital processing system for amplitude-monopulse RSSI-based MiMo WiFi direction-of-arrival estimation," *IEEE J. Sel. Topics Signal Process.*, vol. 12, no. 3, pp. 529–540, Jun. 2018.
[25] D. Bonefačić, J. Jančula, and N. Majurec, "Model of a monopulse radar tracking system for student laboratory," *Radioengineering*, vol. 16, no. 3, pp. 63–67, Sep. 2007.
[26] University of Adelaide. *Project: Inexpensive Portable Radar System*. Accessed: Jun. 2019. [Online]. Available: https://www.eleceng.adelaide.edu.au/students/wiki/projects/index.php/Projects:2015s1-21_Inexpensive_Portable_Radar_System
[27] L. Lo Monte, R. Vela, and L. Westbrook, "Rediscovering monopulse radar with digital sum-difference beamforming," in *Proc. IEEE Int. Symp. Antennas Propag.*, Chicago, IL, USA, Jul. 2012, pp. 1–2.
[28] P. V. S. Pirom and T. Saelim, "RSSI monopulse azimuth tracking demonstration using wideband personal area network device," *Int. J. Eng. Res. Technol.*, vol. 2, no. 9, pp. 663–670, 2013.
[29] M. Poveda-García, J. A. López-Pastor, A. Gómez-Alcaraz, L. M. Martínez-Tamargo, M. Pérez-Buitrago, A. Martínez-Sala, D. Cañete-Rebenaque, and J. L. Gómez-Tornero, "Amplitude-monopulse radar lab using WiFi cards," in *Proc. 48th Eur. Microw. Conf. (EuMC)*, Madrid, Spain, Sep. 2018, pp. 464–467.
[30] Datasheet. *Interline 14 dB Panel Antenna IP-G14-F2425-H*. Accessed: May 2019. [Online]. Available: http://www.interline.pl/antennas/PANEL-14-2.4GHz
[31] C. A. Balanis, *Antenna Theory*. New York, NY, USA: Wiley, 1982.
[32] A. Michel and P. Nepa, "UHF-RFID desktop reader antennas: Performance analysis in the near-field region," *IEEE Antennas Wireless Propag. Lett.*, vol. 15, pp. 1430–1433, 2016.
[33] A. Michel, P. Nepa, X. Qing, and Z. N. Chen, "Considering high-performance near-field reader antennas: Comparisons of proposed antenna layouts for ultrahigh-frequency near-field radio-frequency identification," *IEEE Antennas Propag. Mag.*, vol. 60, no. 1, pp. 14–26, Feb. 2018.

JOSE ANTONIO LÓPEZ-PASTOR received the B.S. degree in telematics engineering, in 2006, and the M.S. degree in telecommunication engineering from the Universidad Politecnica de Cartagena (UPCT), Cartagena, Spain, in 2010. After working eight years in private R&D Technological Center, he started Ph.D. degree with the Technical University of Cartagena (UPCT). His research interests include indoor positioning systems, software programming, and the IoT.

ANTONIO GÓMEZ-ALCARAZ was born in San Javier, Spain, in 1994. He received the degree in telecommunications engineering from the Technical University of Cartagena, Spain, in 2017, where he is currently pursuing the master's degree in telecommunications engineering. His research interests include leaky-wave antennas and their application in telecommunication systems, indoor location systems, and the IoT.

DAVID CAÑETE-REBENAQUE was born in Valencia, Spain, in 1976. He received the degree in telecommunications engineering from the Technical University of Valencia, Valencia, in 2000, and the Ph.D. degree from the Technical University of Cartagena, Cartagena, Spain, in 2009. During 2001, he was an RF Engineer with a mobile communication company. In 2002, he joined the Communications and Information Technologies Department, Technical University of Cartagena, where he is involved in research and teaching activities. He has been an Associate Professor, since 2011. His research interests include the analysis and design of planar microwave circuits and antennas, and their application for radio localization and wireless power transmission.

ALEJANDRO SANTOS MARTINEZ-SALA was born in Cehegin, Spain, in 1976. He received the degree in electrical engineering, and the Ph.D. degree in telecommunications from the Technical University of Cartagena (UPCT), Spain, in 2000 and 2006, respectively. In 2001, he joined UPCT, where he is currently an Assistant Professor with the Communications and Information Technologies Department. His research interests include indoor location systems, wireless sensor networks, and innovation and technology transfer.

JOSÉ LUIS GÓMEZ-TORNERO (S'01–M'06–SM'14) was born in Murcia, Spain, in 1977. He received the degree in telecommunications engineering from the Technical University of Valencia, Valencia, Spain, in 2001, and the Ph.D. degree from the Technical University of Cartagena (UPCT), Cartagena, Spain, in 2005.

In 2000, he joined the Radio Frequency Division, Industry Alcatel Espacio, Madrid, Spain. In 2001, he joined UPCT, where he has been an Associate Professor, since 2008. He was the Vice Dean for Students and Lectures affairs as a member of the Telecommunication Engineering Faculty. He has been a Visiting Researcher/Professor with the University of Loughborough, Loughborough, U.K., Heriot-Watt University, Edinburgh, U.K., Queen's University of Belfast, Belfast, U.K., and CSIRO-ICT Centre, Sydney, NSW, Australia. In 2010, he was appointed as a CSIRO Distinguished Visiting Scientist by the CSIRO ICT Centre. He has coauthored more than 50 peer-reviewed journal papers, and more than 100 conference papers. His current research interests include the analysis and design of leaky-wave devices and their applications, and the innovation in the area of higher education. His research work has received various awards, including the EPSON-Ibérica Foundation (2004) and Vodafone Foundation (2005) awards to the Best Ph.D. Thesis in the area of advanced mobile communications technologies, Hispasat (2014) and Hisdesat (2015) prizes to the Best Ph.D. Thesis in Satellite Communication technologies. Also, he was a co-recipient of the 2010 IEEE Engineering Education Conference Award, the 2011 EuCAP Best Student Paper Prize, the 2012 EuCAP Best Antenna Theory Paper Prize, the 2012 and 2013 Spanish URSI Prize for the Best Student Paper, the 2013 APS Best Student Paper Finalist, and the 2018 iWAT Best Poster Award.